remote sensing

MDPI

Communication

Real-Time Water Level Monitoring Based on GNSS Dual-Antenna Attitude Measurement

Pengjie Zhang [1,2], Zhiguo Pang [1,2,*,†], Jingxuan Lu [1,2], Wei Jiang [1,2,†] and Minghan Sun [1,2]

[1] State Key Laboratory of Simulation and Regulation of Water Cycle in River Basin, China Institute of Water Resources and Hydropower Research, Beijing 100038, China; zhangpengjie@edu.iwhr.com (P.Z.); lujx@iwhr.com (J.L.); jiangwei@iwhr.com (W.J.); sunminghan@edu.iwhr.com (M.S.)
[2] Research Center of Flood and Drought Disaster Reduction of the Ministry of Water Resources, Beijing 100038, China
* Correspondence: pangzg@iwhr.com
† These authors contributed equally to this work.

Abstract: Real-time and high-precision water level monitoring is crucial for the fields of hydrology, hydraulic engineering, and disaster prevention and control. The most prevalent method for measuring water level is through the use of water level gauges, which can be costly and have limited coverage. In recent years, Global Navigation Satellite System Reflectometry (GNSS-R) technology has emerged as a promising approach for water level monitoring due to its low cost and high coverage. However, a limitation of current GNSS-R technology is the extended time required to record signals, which hinders its potential for real-time application. This paper introduces a novel real-time water level monitoring method based on GNSS dual-antenna attitude measurement and develops a model to invert water level based on baseline vector. This method uses double-difference observations to eliminate errors caused by various factors, such as satellite and receiver clock, and ionospheric and tropospheric delay. To avoid the impact of detecting and correcting cycle slips during real-time operations, a single-epoch calculation method is introduced. In order to verify the stability and reliability of our method, field tests were carried out at Dongshahe Station in Beijing. We obtained water level data with a time resolution of 1 Hz through field experiments. Experimental data collected from 12 May to 8 June 2022 and from 4 July to 8 August 2022 showed good agreement with on-site water gauge measurements, with root mean square errors of 2.77 cm and 2.54 cm, respectively. Experimental results demonstrate that this method can achieve high-precision, high-temporal-resolution water level monitoring.

Keywords: GNSS-R; GNSS dual-antenna attitude measurement; water level

check for updates

Citation: Zhang, P.; Pang, Z.; Lu, J.; Jiang, W.; Sun, M. Real-Time Water Level Monitoring Based on GNSS Dual-Antenna Attitude Measurement. *Remote Sens.* **2023**, *15*, 3119. https://doi.org/10.3390/rs15123119

Academic Editors: Nereida Rodriguez-Alvarez, Mary Morris and Joan Francesc Munoz-Martin

Received: 17 April 2023
Revised: 2 June 2023
Accepted: 7 June 2023
Published: 14 June 2023

Copyright: © 2023 by the authors. Licensee MDPI, Basel, Switzerland. This article is an open access article distributed under the terms and conditions of the Creative Commons Attribution (CC BY) license (https://creativecommons.org/licenses/by/4.0/).

1. Introduction

The Global Navigation Satellite System (GNSS) not only provides navigation, positioning, and timing services to users worldwide but also continuously transmits massive high temporal-spatial resolution and high-precision microwave signals (especially the 1–2 GHz L-band signals) to the Earth's surface [1]. Through GNSS studies, researchers have discovered that GNSS-reflected signals carry characteristic information about the reflective surface. Using GNSS-reflected signals, it is possible to estimate and retrieve the physical characteristics of reflective surfaces without a special radar transmitter [2]. This has led to the emergence of GNSS-R, an interdisciplinary field of GNSS and remote sensing. GNSS-R offers benefits such as low cost, low power consumption, and high temporal resolution compared to traditional satellite microwave remote sensing. In recent decades, with the continuous improvement of the theoretical architecture system, signal processing technology, and parameter retrieval model of GNSS-R, it has made some progress in fields such as ocean surface wind [3], ocean altimetry [4], sea ice [5], soil moisture [6], etc.

Water level monitoring has always been crucial in hydrology and water resources, and water conservancy engineering management. In recent years, traditional manual water gauges have been replaced with float-type, pressure-type, ultrasonic, and other types of water level gauges, resulting in significant improvements in automation and measurement accuracy to meet general water level monitoring requirements. However, these methods have low coverage, particularly in complex terrains, such as high slopes in reservoir areas and harsh weather conditions, which can hinder their accuracy, reliability, and availability [7]. To address this issue, GNSS-R provides a new approach to achieve high coverage water level monitoring with its unique advantages. In 1993, Martin-Neira first proposed the concept of Passive Reflectometry and Interferometry System (PARIS) and demonstrated the feasibility of using GPS reflection signals for altimetry [8]. Subsequently, various scholars conducted experimental studies to ascertain the viability of using GNSS-R technology for measuring water levels [9–11]. After over two decades of development, GNSS-R altimetry has been proven to be effective for water level retrieval in oceans [12], lakes [13], rivers [14], and reservoirs [15].

Currently, there are three commonly used methods in GNSS-R altimetry. The first is code-delay altimetry, which determines a time delay between the direct and reflected signals' peaks and then retrieves the water level based on this delay. The C/A code of GPS and the B1I code of BDS can be used to invert sea surface height with high spatial and temporal resolution [16]. However, due to the relatively narrow bandwidth of GNSS signals, accuracy using this method is limited to the meter level [17]. The second altimetry method, proposed by Larson et al. in 2013, utilizes signal-to-noise (SNR) ratio data. This method retrieves water level by processing signal-to-noise ratio data containing interference information from GNSS direct and reflected signals [18]. Numerous studies have demonstrated that the oscillation frequency of multipath in SNR data correlates with the height of the antenna above the reflecting surface [19–21]. They achieved millimeter-level accuracy in water level inversion for the first time by combining data from multiple stations and signals [22]. However, this method requires long continuous recording time and can only use GNSS signals from satellites with low elevation angles. As a result, its temporal resolution is low [23]. The third method is carrier phase delay altimetry, which confirms the path delay between direct and reflected signals using carrier phase observations [24]. In comparison to SNR analysis, phase altimetry not only enables centimeter-level sea-level altitude inversion but also provides high temporal resolution [25]. However, when the sea surface is rough, the continuity of the reflected signal phase is disrupted, making it difficult to track [26]. In contrast to complex sea conditions, the water surface of inland water bodies is relatively calm. This makes the characteristics of the reflected signals more stable and their phase information easier to measure accurately. As a result, this paper focuses on the carrier phase altimetry technique.

The key to phase altimetry is resolving the integer ambiguity. However, this is a complex problem. Scholars have proposed methods to avoid calculating the integer ambiguity [27–29], and these methods can achieve a temporal resolution of up to 1 min. Nonetheless, during emergency situations such as flash floods, water authorities require even higher temporal resolution of water level data to effectively develop emergency response measures. Lifeng Bao and colleagues achieved 1 Hz temporal resolution and 1 cm accuracy in water level monitoring by introducing an atomic clock [30]. However, the high cost of atomic clocks limits their practical application. To address these issues, this paper investigates real-time water level monitoring using GNSS dual-antenna attitude measurement. In recent years, GNSS dual-antenna attitude measurement has played an important role in real-time carrier attitude measurement with the advantages of low cost, high accuracy, short initialization time and high reliability. GNSS dual-antenna attitude measurement determines the relative direction and distance between two antennas by measuring the phase difference between different GNSS signals [31]. So GNSS dual antenna attitude measurement algorithm can be used to achieve real-time monitoring of water level.

When the water surface is rough, the reflected signal may lose its lock and exhibit cycle slips phenomenon. In GNSS-R carrier phase altimetry, cycle slips can significantly impact the accuracy of water level monitoring [32]. However, detecting and correcting cycle slips is time-consuming and not well-suited for real-time applications. GNSS single-epoch calculation is a positioning technique that processes satellite measurement data at a single time point. GNSS single-epoch calculation is not affected by cycle slips and allows for immediate reinitialization after satellite signal loss. In harsh observation environments, single-epoch calculation offers higher data availability compared to multiple-epoch data, enabling the efficient utilization of observation data. To avoid the impact of cycle slips on real-time applications, this study introduces a single-epoch calculation method. When the reflected signal enters the right-hand circularly polarized (RHCP) antenna, signal crosstalk will occur [33]. Dallas Masters installed signal clapboards between the RHCP and left-hand circular polarized (LHCP) antennas to mitigate the impact of signal crosstalk on the carrier phase [34]. Inspired by his work, we installed a signal clapboard at the midpoint of the connection axis between the RHCP and LHCP antennas.

The primary aim of this paper is to enhance the temporal resolution of GNSS-R phase altimetry, thereby facilitating its widespread implementation in practical scenarios. We present a novel approach for real-time water level monitoring using GNSS dual-antenna attitude measurement and develop a model to retrieve water level based on baseline vector. For the first time, this approach determines the position of the virtual antenna using the attitude angle information of the baseline vector. This approach offers a new idea for monitoring water levels in remote areas, including key lakes and rivers.

2. Methodology

2.1. Program Design

Figure 1 shows the flow of the real-time water level monitoring algorithm based on GNSS dual-antenna attitude measurement. Firstly, the GNSS data received by the two antennas are parsed to extract the valid data from them. The satellite position and receiver position are decoded from GNSS data. Then, the Geometric Dilution of Precision (GDOP) [35] satellite selection algorithm is used to obtain the best combination of satellites for attitude solution, and the observed elevation angles of all satellites in the combination are calculated. The satellite with the highest observation elevation angle is selected as the reference satellite, and the attitude measurement observation model is established. Using the weighted least squares method to solve the observation model, the float solution of the baseline vector and the integer ambiguity can be obtained. Next, the Least-Squares Ambiguity Decorrelation Adjustment (LAMBDA) [36] algorithm is applied to the float solution to search for ambiguities and obtain a fixed integer ambiguity. The fixed integer ambiguity is then used to correct the baseline vector's float solution, resulting in a corrected baseline vector. Subsequently, the attitude solution algorithm can be used to determine the length, azimuth and pitch angle of the baseline formed by the two antennas. Finally, the water level is calculated using the baseline length.

2.2. Altimetry Principle

In the GNSS dual antenna attitude measurement-based water level monitoring method, the right-hand circularly polarized (RHCP) antenna is installed skyward to receive direct GNSS satellite signals. The left-hand circularly polarized (LHCP) antenna is installed towards the water to receive GNSS signals reflected from the water surface. The phase centers of both antennas are aligned on the same plumb line. Figure 2 illustrates a schematic diagram depicting the geometric relationship of the GNSS dual-antenna attitude measurement-based water level monitoring method. As shown in Figure 2, the positions of the RHCP and LHCP antennas remain unchanged. Compared to the direct signal received by the RHCP antenna, the reflected signal received by the LHCP antenna has an additional propagation path. As such, the LHCP antenna can be considered a virtual antenna located beneath the water surface. The distance between the virtual antenna and the water surface is

equal to the distance between the LHCP antenna and the water surface. When the water surface height changes, the additional propagation path of the reflected signal also changes. Consequently, the position of the virtual antenna changes accordingly. As a result, the GNSS dual-antenna attitude measurement technique can be used to calculate the baseline length between the RHCP and LHCP antennas in real-time.

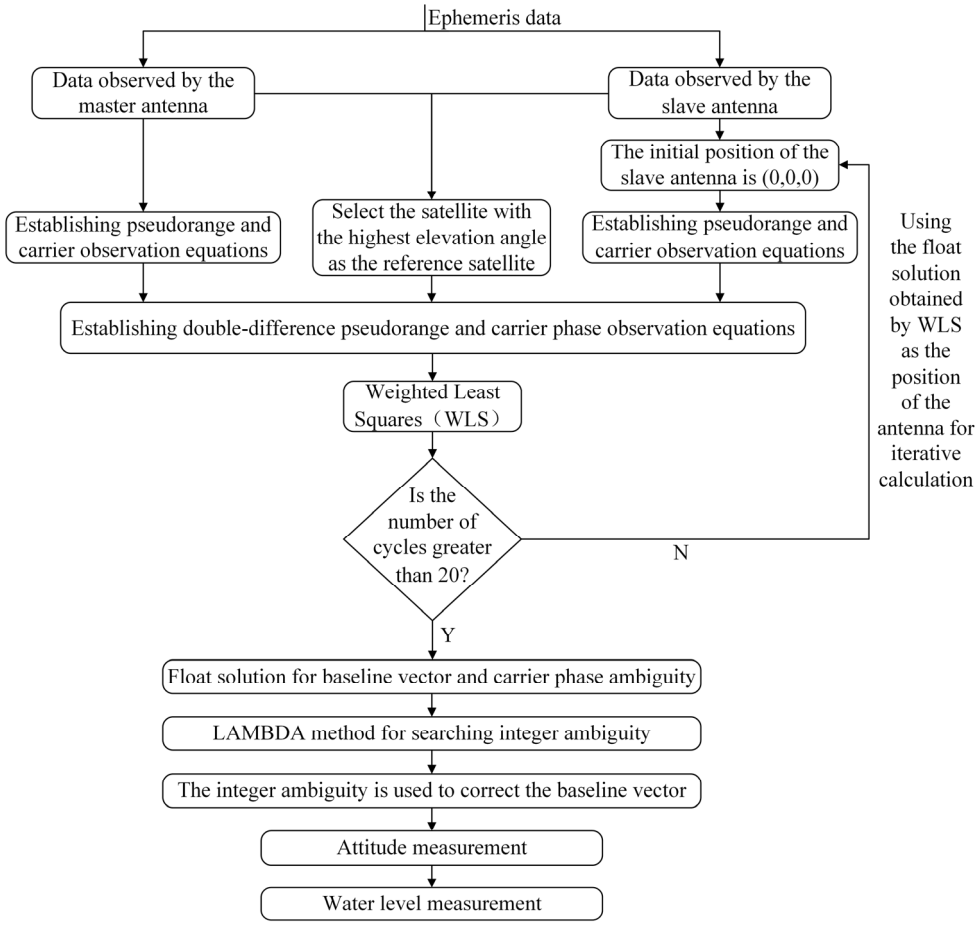


Figure 1. Flow chart of real-time water level monitoring method based on GNSS dual antenna attitude measurement.

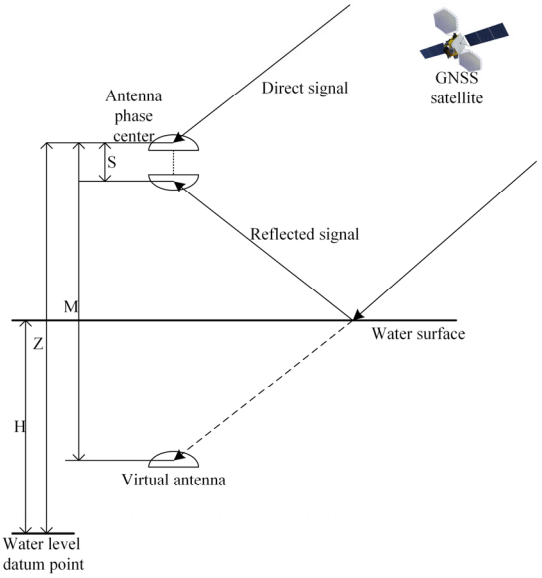


Figure 2. Geometry of the GNSS-R experiment.

As shown in Figure 2, the water surface height is related to the baseline length between the two antennas. This relationship can be derived from their geometric relationship:

$$H = Z - \left(\frac{M - S}{2} + S\right) \tag{1}$$

where, H is the water surface height; Z is the measured distance from the antenna phase center to the water reference point; M is the baseline length; and S is the measured distance between the sky observation antenna and the water observation antenna.

2.3. Baseline Vector Calculation

GNSS provides various observables including pseudorange, carrier phase and Doppler [37,38]. Pseudorange and carrier phase are commonly used in GNSS attitude measurement systems. Equations (2) and (3) represent the pseudorange and carrier phase observation equations, respectively.

$$P_m^j = \rho_m^j + c\cdot\left(\delta t_{u,m} - \delta t^j\right) + T_m + I_m + \varepsilon_{P_m} \tag{2}$$

$$\phi_m^j = \lambda\cdot\varphi_m^j = \rho_m^j + c\cdot\left(\delta t_{u,m} - \delta t^j\right) + T_m - I_m + \lambda\cdot N_m + \varepsilon_{L_m} \tag{3}$$

where, P_m^j is the pseudorange observation between antenna m and satellite j, ϕ_m^j is the carrier phase observation between antenna m and satellite j, ρ_m^j is the geometric distance between antennas m and satellite j, $\delta t_{u,m}$ is the receiver clock error, δt^j is the satellite clock error, T_m is the tropospheric delay, I_m is the ionospheric delay, N_m is the carrier-phase integer ambiguity, c is the speed of light, λ is the signal carrier wavelength, ε_{P_m} and ε_{L_m} are the observation noise of pseudorange and carrier, respectively.

To reduce various errors in positioning, we use a double-difference observation combination. The expressions are as follows:

$$\nabla\Delta P_{sm}^{jk} = \nabla\Delta\rho_{sm}^{jk} + \nabla\Delta\varepsilon_{P_{sm}^{jk}} \tag{4}$$

$$\nabla\Delta\phi_{sm}^{jk} = \nabla\Delta\rho_{sm}^{jk} + \lambda\cdot\nabla\Delta N_{sm}^{jk} + \nabla\Delta\varepsilon_{L_{sm}^{jk}} \tag{5}$$

where, s represents antenna s, m represents antenna m, j represents satellite j, and k represents satellite k, $\nabla\Delta P_{sm}^{jk}$ is the pseudorange double difference, $\nabla\Delta\rho_{sm}^{jk}$ is the double difference of the geometric distance between the antenna and the satellite, $\nabla\Delta\phi_{ms}^{jk}$ is the carrier phase double difference, $\nabla\Delta N_{sm}^{jk}$ is the integer ambiguity double difference, $\nabla\Delta\varepsilon_{P_{sm}^{jk}}$ and $\nabla\Delta\varepsilon_{L_{sm}^{jk}}$ are the observed noise double differences of pseudorange and carrier, respectively. Under short baseline conditions, most errors in observed quantities such as satellite orbit and clock differences, ionospheric and tropospheric delays, and receiver clock differences are eliminated after applying the double-difference combination.

Assuming antenna s serves as the primary antenna, located approximately at (x_0, y_0, z_0), the linear expansion process of the distances ρ_s^j and ρ_s^k between antenna s and the satellite at (x_0, y_0, z_0) can be expressed as:

$$\widetilde{\rho}_s^j = \rho_0^j \tag{6}$$

ρ_0^j can be further expressed as:

$$\rho_0^j = \sqrt{\left[\left(X^j - X_0\right)^2 + \left(Y^j - Y_0\right)^2 + \left(Z^j - Z_0\right)^2\right]} \tag{7}$$

Similarly, the linear expansion process of ρ_m^j and ρ_m^k of antenna m at (x_0, y_0, z_0) can be expressed as:

$$\widetilde{\rho}_m^j = \rho_0^j - \frac{X^j - x_0}{\rho_0^j}dx - \frac{Y^j - y_0}{\rho_0^j}dy - \frac{Z^j - z_0}{\rho_0^j}dz \tag{8}$$

where (dx, dy, dz) represents the distance between the antenna m to the approximate position of the antenna s. This distance is the baseline vector between the two antennas. Let us redefine the variables as follows:

$$h_x^j = \frac{X^j - x_0}{\rho_0^j}, h_y^j = \frac{Y^j - y_0}{\rho_0^j}, h_z^j = \frac{Z^j - z_0}{\rho_0^j} \tag{9}$$

Equation (8) can be further expressed as:

$$\widetilde{\rho}_m^j = \rho_0^j - \begin{bmatrix} h_x^j & h_y^j & h_z^j \end{bmatrix} \times \begin{bmatrix} dx \\ dy \\ dz \end{bmatrix} \tag{10}$$

$\widetilde{\rho}_m^k$ can be obtained in the same way. According to Equations (6) and (7), $\widetilde{\rho}_s^{jk}$ and $\widetilde{\rho}_m^{jk}$ can be, respectively, expressed as:

$$\widetilde{\rho}_s^{jk} = \rho_0^j - \rho_0^k \tag{11}$$

$$\widetilde{\rho}_m^{jk} = \rho_0^j - \rho_0^k - \begin{bmatrix} h_x^{jk} & h_y^{jk} & h_z^{jk} \end{bmatrix} \times \begin{bmatrix} dx \\ dy \\ dz \end{bmatrix} \tag{12}$$

where $h_x^{jk} = h_x^j - h_x^k$, $h_y^{jk} = h_y^j - h_y^k$, $h_z^{jk} = h_z^j - h_z^k$. Based on the above, we can obtain:

$$\nabla\Delta\widetilde{\rho}_{sm}^{jk} = \Delta\widetilde{\rho}_s^{jk} - \Delta\widetilde{\rho}_m^{jk} = \begin{bmatrix} h_x^{jk} & h_y^{jk} & h_z^{jk} \end{bmatrix} \times \begin{bmatrix} dx \\ dy \\ dz \end{bmatrix} \tag{13}$$

By linearizing Equations (4) and (5), we obtain the following equations:

$$y = A \cdot a + B \cdot b + e \tag{14}$$

where, y is the GNSS observation vector, A is the design containing the carrier wavelengths, B is the design matrix of unit line-of-sight vectors, a is the integer ambiguity vector, b is the baseline vector, e is the observation error vector.

By ignoring the integer property of the integer ambiguity, we can solve for the float solution of the integer ambiguity parameters a and other unknown parameters b using the least squares method. Their variance covariance array can also be obtained, and the results are denoted as follows:

$$\begin{bmatrix} \hat{a} \\ \hat{b} \end{bmatrix}; \begin{bmatrix} Q_{\hat{a}} & Q_{\hat{b}\hat{a}} \\ Q_{\hat{a}\hat{b}} & Q_{\hat{b}} \end{bmatrix} \tag{15}$$

2.4. Fixing of Integer Ambiguity

The carrier phase measurement in GNSS should ideally result in an integer number of cycles around the whole perimeter, but due to measurement imprecision, the least squares method may yield a fractional number. In order to obtain a more accurate integer solution, the LAMBDA algorithm can be employed to search for the nearest integer value of the obtained float point solution, thus providing a fixed whole perimeter integer ambiguity resolution. The search space for the integer ambiguity is defined as follows:

$$\Omega_a = \{a \in Z^n | (\hat{a} - a)^T \cdot Q_{\hat{a}}^{-1} \cdot (\hat{a} - a) \leq \chi^2\} \tag{16}$$

where χ^2 is a chosen positive constant, The boundary of this search space is an ellipsoidal plane with its center at â. The shape of the ellipsoid is determined by $Q_{\hat{a}}$ and its size is determined by χ^2. To improve search efficiency, the LAMBDA method applies a decorrelation transformation as follows:

$$z = Z^T \cdot a;\ Q_{\hat{z}} = Z^T \cdot Q_{\hat{a}} \cdot Z;\ \hat{z} = Z^T \cdot \hat{a} \tag{17}$$

where z and $Q_{\hat{z}}$ are the vectors of a and $Q_{\hat{a}}$ after integer transformation, respectively. The Z-transformed search space is as follows:

$$\Omega_a = \{z \in Z^n | (\hat{z} - z)^T \cdot Q_{\hat{z}}^{-1} \cdot (\hat{z} - z) \leq \chi^2\} \tag{18}$$

The ambiguity search is then conducted in the new space. The correct ambiguities identified are transformed back into the original space using Equation (17) to obtain the integer ambiguity.

The float solution of the baseline vector is adjusted by applying a fixed integer ambiguity. The baseline is corrected as follows:

$$b = \hat{b} - Q_{\hat{b}\hat{a}} \cdot Q_{\hat{a}}^{-1} (\hat{a} - a) \tag{19}$$

$$Q_b = Q_{\hat{b}} - Q_{\hat{b}\hat{a}} \cdot Q_{\hat{a}}^{-1} \cdot Q_{\hat{a}\hat{b}} \tag{20}$$

After obtaining the fixed solution for the integer ambiguity, its reliability must be verified. Methods for confirming integer ambiguity include the F-Ratio test [39], R-Ratio test [40], difference test [41], and projection test [42]. In practice, the R-Ratio test is the simplest and most commonly used method [43].

2.5. Definition and Calculation of Attitude Angle

2.5.1. Definition of Attitude Angle

The carrier attitude angle refers to the angular relationship between a carrier's own coordinate system (Body-Fixed coordinate system) and the Local Level coordinate system (LLS). It is typically represented by a set of attitude angles: heading, pitch, and roll. Since this study employs a single baseline measurement, only the heading and pitch angles of the carrier can be measured. Figure 3 shows the heading angle y as the angle between the projection of the carrier's main baseline vector on the LLS and the Y-axis of the LLS. The pitch angle p is the angle between the carrier's main baseline vector and the XOY plane of the LLS. The roll angle r is the angle between the X_B axis along the Body-Fixed coordinate system and the XOY plane of the LLS.

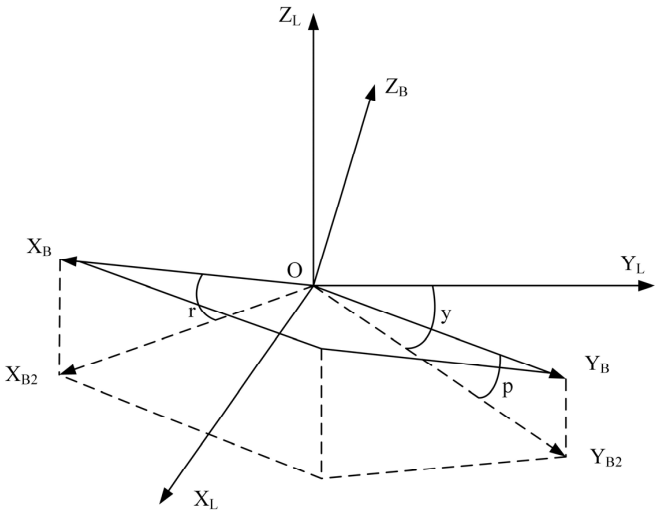


Figure 3. Definition of Heading, Pitch and Roll.

2.5.2. Calculation of Attitude Angle

Assuming that the coordinates $\begin{bmatrix} x & y & z \end{bmatrix}^T$ of the baseline vector at time 't' are obtained in the WGS-84 coordinate system, the coordinates $\begin{bmatrix} e & n & u \end{bmatrix}^T$ of the baseline vector in the local horizontal coordinate system can be determined using a coordinate conversion relationship. The specific conversion formula is as follows:

$$\begin{bmatrix} e & n & u \end{bmatrix}^T = S\begin{bmatrix} x & y & z \end{bmatrix}^T \tag{21}$$

where S is the coordinate transformation matrix.

$$S = \begin{bmatrix} -\sin\lambda & \cos\phi & 0 \\ -\sin\phi\cos\lambda & -\sin\phi\sin\lambda & \cos\phi \\ \cos\phi\cos\lambda & \cos\phi\sin\lambda & \sin\phi \end{bmatrix} \tag{22}$$

where λ and ϕ are the longitude and latitude of the main antenna at time 't', respectively. The heading and pitch angles of the carrier can be calculated according to the definition of attitude angle using the following equations:

$$y = -\arctan\left(\frac{e}{n}\right) \tag{23}$$

$$p = \arcsin\left(\frac{u}{\sqrt{e^2 + n^2}}\right) \tag{24}$$

where y and p represent the heading and pitch angles, respectively.

3. Field Experiment

3.1. Experimental Scenario

On 12 May 2022, an experiment was conducted at the Dongshahe Station of the Beijing Longshan Administration, located at coordinates 40°11′25.59″N and 116°15′11.55″E. Figure 4 shows the equipment installation location during the experiment, where no obstructions were present above the site and the water surface was calm. To mitigate the reception of reflected signals from the grass and surrounding buildings at the experimental site, we impose an azimuth limitation for the satellites considered in the calculation, restricting them to the range of 45° to 250°. The receiver equipment was housed in a cabinet, and a solar power system was closely connected to the cabinet. The field experiment data were transmitted to a monitoring platform using 4G technology.

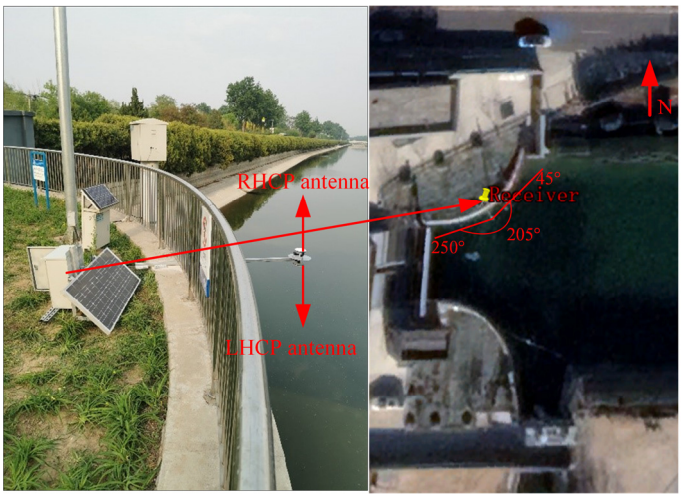


Figure 4. GNSS-R experiment setup at Dongshahe station.

The signal emitted by GNSS satellites is a RHCP signal. After reflecting off the water surface, it changes to a signal dominated by left-hand circular polarization. The higher the elevation angle of the satellite, the larger its left-hand circular polarization ratio. The left-hand circularly polarized antenna is suitable for receiving reflected signals with an elevation angle greater than 20° [44]. Therefore, in our experiment, we set the satellite cut-off elevation angle to 20°. Equation (13) contains three unknown parameters. Therefore, to solve these unknowns, at least four or more satellites must be observed simultaneously. Figure 5 displays a 24 h GNSS sky plot observed at the experimental site on 10 July 2022. As shown in Figure 5, the number of available reflections with elevation angles above 20° and azimuth angles within the range of 45° to 250° is sufficient to meet the calculation requirements.

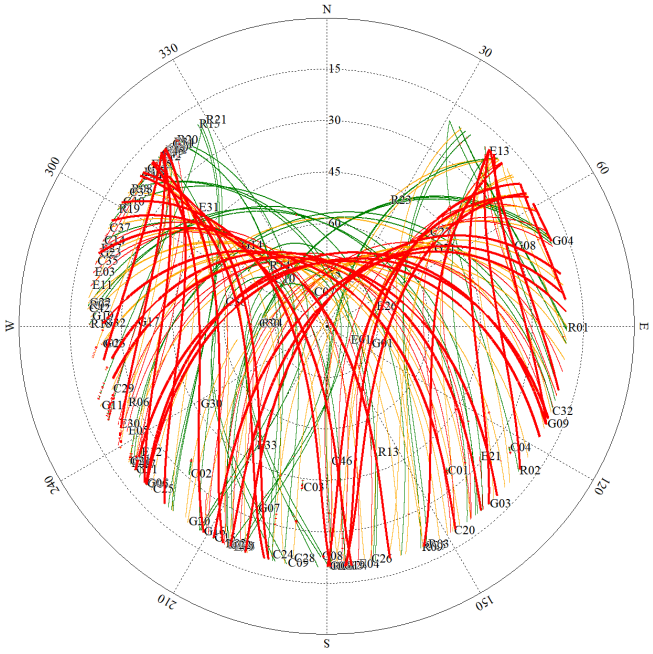


Figure 5. Sky plot of GNSS for 24 h on 10 July 2022.

To determine the height of the antenna connecting rod above the water surface, the steel tape measure was used ten times, and the average height was found to be 3.03 m. Figure 6 illustrates the location of the water gauge at the experimental site, which confirmed the water depth at this location to be 1.08 m. The final height of the antenna connecting rod above the water level reference point (the zero point at the bottom of the water gauge) was calculated to be 4.11 m. To compare and validate our experimental results, water level data obtained by the site staff through the water gauge were collected at 07:30, 15:30, and 18:30 daily.



Figure 6. The water level at the experimental site was obtained using a water gauge.

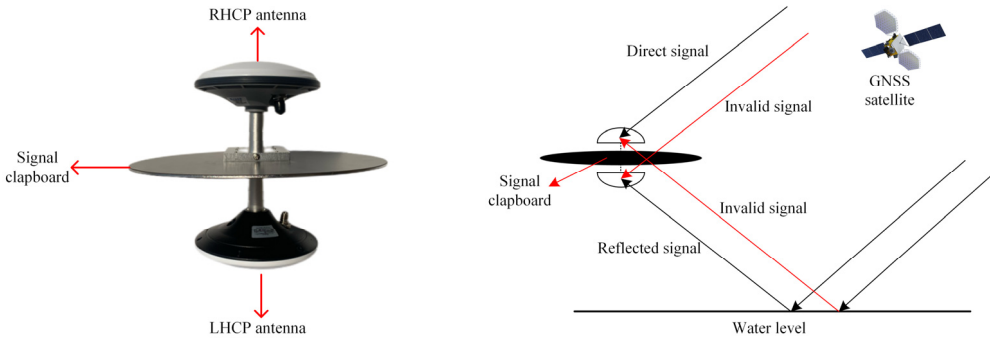
3.2. Experimental Equipment

The receiver used in the experiment was jointly developed by the China Institute of Water Resources and Hydropower Research and Shanghai Sinan Satellite Navigation Technology Company Limited. The receiver supports BeiDou global signals and other mainstream global satellite navigation systems.

Table 1 presents the parameters of the antennas used in this experiment. Figure 7a depicts the antennas used in this experiment. The RHCP antenna receives the direct satellite signal, and the LHCP antenna receives the reflected signal from the water surface. We positioned a signal clapboard at the midpoint of the connection axis between the RHCP and LHCP antennas. The signal clapboard was covered with wave-absorbing material, and its projected area on both antennas was larger than their corresponding antenna areas. As shown in Figure 7b, the clapboard reduces interference from water surface-reflected satellite signals on the RHCP antenna and from direct satellite signals on the LHCP antenna.

Table 1. Parameters of RHCP and R-RHCP antennas.

Types of Antennas	RHCP Antenna	LHCP Antenna
Operating temperature	−40 °C~+70 °C	−40 °C~+70 °C
Antenna gain	40 ± 2 dB	40 ± 2 dB
Working frequency	BDS B1/B2/B3	BDS B1/B2/B3
	GPS L1/L2/L5	GPS L1/L2/L5
	GLONASS L1/L2	GLONASS L1/L2
	GALILEO E1/E5a/E5b	GALILEO E1/E5a/E5b
	L-Band	L-Band
	SBAS	SBAS
Phase center error	±2 mm	±2 mm
Weight	≤500 g	≤500 g
Size	Φ147 × 67.7	Φ147 × 67.7



(**a**) (**b**)

Figure 7. Dual antennas in the experiment. (**a**) Vertical upward RHCP antenna, vertical downward LHCP antenna and signal clapboard; (**b**) The signal clapboard prevents the RHCP antenna from receiving reflected signals from the water surface and the LHCP antenna from receiving direct signals from satellites.

4. Results

4.1. Variation of Water Surface Height

Through our experiments, we obtained water level data at 1 s intervals from 12 May to 8 June 2022 and from 4 July to 8 August 2022. Unfortunately, data for certain time periods is unavailable due to equipment and network issues. Figure 8 displays a scatter plot of water level changes, obtained using the double difference method with a time interval of

1 s, during the period from 4 July to 8 August. To validate the accuracy of our experimental results, we compared them with water level data recorded by on-site staff using a water gauge. On-site staff were required to record water level data daily at 7:30, 15:30, and 18:30. While the staff cannot guarantee the precise recording of the water level at the specified moment, its margin of error will not exceed ten minutes. To reduce errors caused by time asynchrony, we selected water level data from 07:25 to 07:35, 15:25 to 15:35 and 18:25 to 18:35 each day for sliding average filtering. The average value was then taken as the water level data for the corresponding moment.

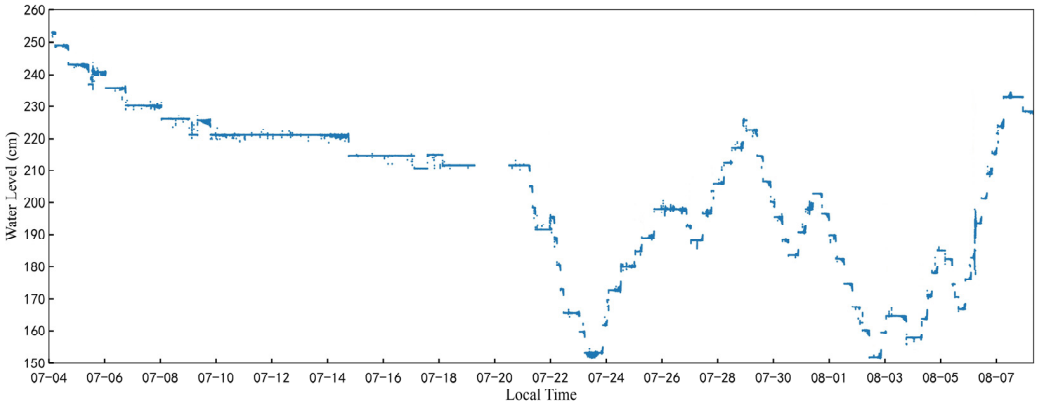


Figure 8. Water level changes, obtained using the double difference method at 1 s intervals, were observed during the period from 4 July to 8 August.

Figures 9 and 10 present the combined results of the experiments conducted from 12 May to 8 June 2022 and from 4 July to 8 August 2022, respectively. The results include the 1 s experimental data, the experimental data smoothed over a 10 min interval, and the readings obtained using a water gauge. As shown in Figures 9 and 10, the trends of GNSS-R altimetry data and water gauge data are generally consistent. The root mean square errors (RMSE) between the 1 s water level data, 10 min averaged water level data, and the readings obtained using a water gauge for the period from 12 May to 8 June 2022, are 2.77 cm and 2.69 cm, respectively. The RMSE between the 1 s water level data, 10 min averaged water level data, and the readings obtained using a water gauge for the period from 4 July to 8 August 2022, are 2.54 cm and 2.49 cm, respectively. The results demonstrate that real-time water level monitoring with centimeter-level accuracy can be achieved through the water level monitoring method based on GNSS dual-antenna attitude measurement. The RMSE results indicate that averaging the water level data over a 10 min period can reduce the error caused by time asynchrony.

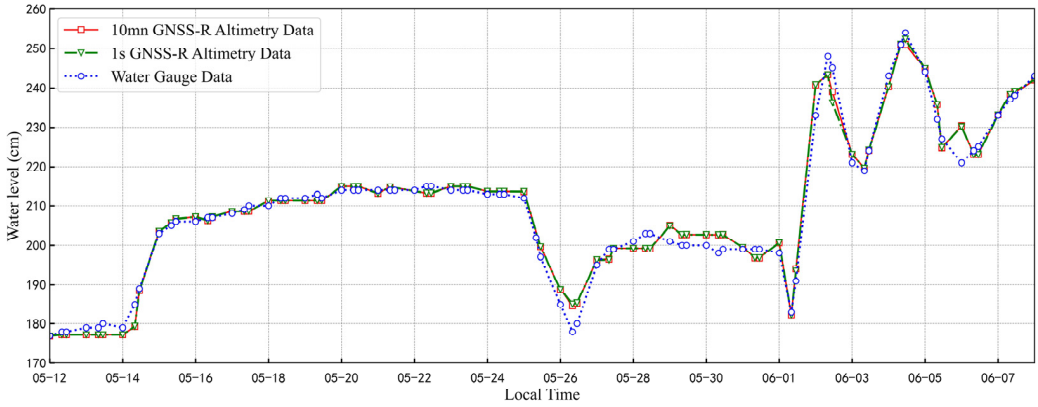


Figure 9. Water level changes for the period from 12 May to 8 June 2022.

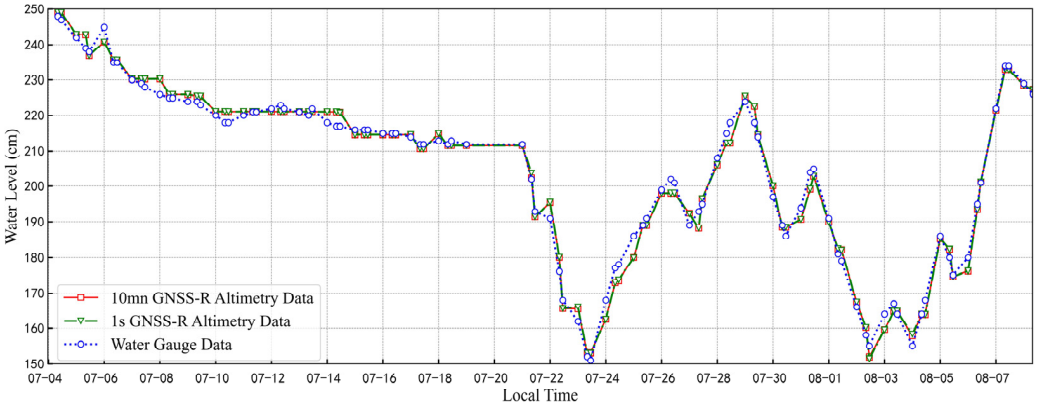


Figure 10. Water level changes for the period from 4 July to 8 August 2022.

4.2. Variation of Attitude Angle

We recorded the heading and pitch angles of the baselines formed by the two antennas during the period from 4 July to 8 August 2022. Figure 11 depicts scatter plots of changes in heading angle and pitch angle during this period. As shown in Figure 11, the heading angle varies from 0° to 360° and the pitch angle varies from −89° to −90°. However, since there is no horizontal distance between the two antennas, the heading angle obtained is not practically meaningful. As shown in Figure 2, when specular reflection occurs through the water surface, the incident angle of the satellite signal is equal to the outgoing angle. At this time, the position of the virtual antenna is located directly below the RHCP antenna, and the pitch angle of the baseline vector between the two antennas is −90°. However, electromagnetic waves can only undergo specular reflection under ideal conditions. In practical experimental environments, this situation does not occur. Therefore, we refer to the position of the virtual antenna at a pitch angle of −90° as the position of the virtual antenna under ideal conditions.

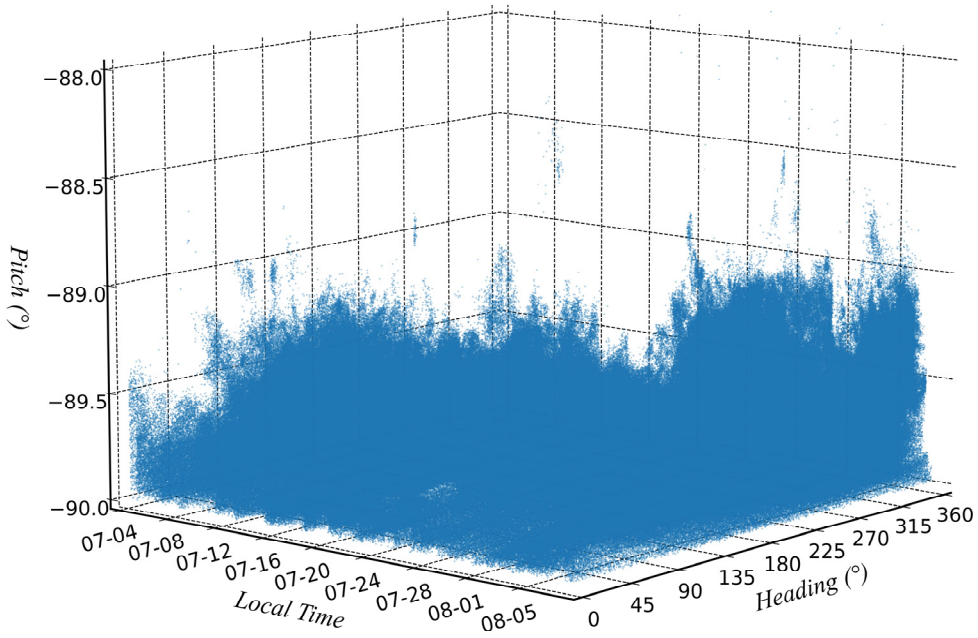


Figure 11. Variations in Heading and Pitch Angles from 4 July to 8 August 2022.

The reasons for the deviation of the pitch angle from −90°, as obtained by double-difference calculations, are as follows: (1) Multi-path effect: In the real situation, the roughness of the water surface is constantly changing due to factors such as wind, currents, and waves. This means that the reflected signal from the water surface will also be constantly changing, producing a large number of reflected signals from the same satellite.

These reflected signals can enter the receiving antenna from various angles and directions, resulting in multiple reflection paths. Each path generates an independent signal with different propagation times and phase delays. These signals may interfere with or superimpose on one another to produce a multi-path effect. (2) Baseline length: Longer baseline lengths can enhance attitude measurement accuracy due to the ability to generate larger distance differences [45], which in turn produce greater phase differences. This increased phase difference allows for more precise measurements, leading to higher accuracy in determining the attitude. (3) Satellite geometry configuration: The position and distribution of satellites in the satellite constellation also impact attitude measurement accuracy. When the satellite distribution is sparse, or the geometric configuration is poor, it can lead to decreased accuracy in attitude measurements. (4) Thermal noise and local oscillator-induced noise can significantly impact the received signal quality in GNSS receivers. These noise sources have the potential to introduce uncertainties in the measurement data, thereby affecting the accuracy of the results. The errors in the least-squares estimation encompass various factors such as initial state estimation errors, process noise, and measurement noise. These errors tend to accumulate during the estimation process and can subsequently influence the accuracy of the attitude measurements.

As illustrated in Figure 12, the position of the virtual antenna determined using the pitch angle deviates from its ideal position. To calculate the water level, the vertical distance between the two antennas is required. However, the baseline length recorded by the receiver represents the distance between the RHCP antenna and the actual virtual antenna.

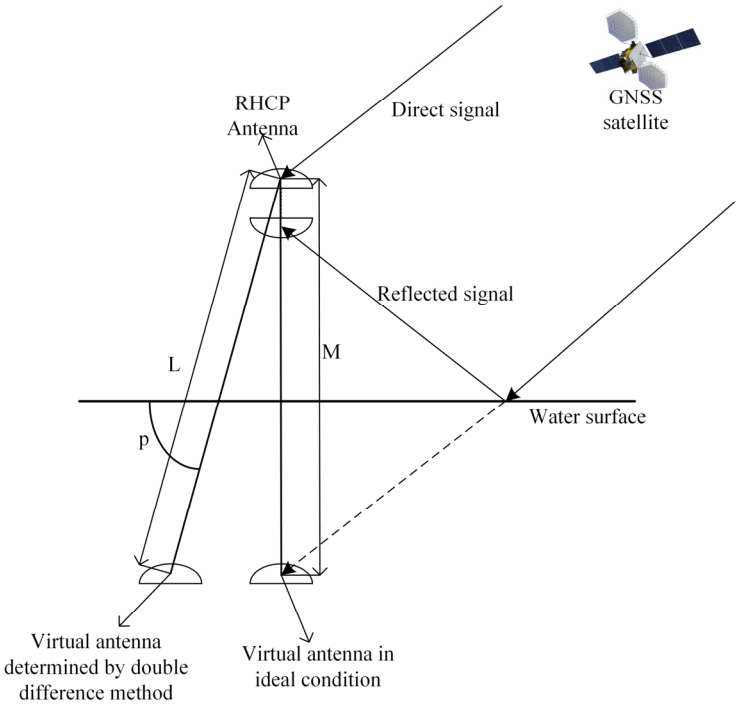


Figure 12. The position of the virtual antenna is determined from the pitch angle and its position in the ideal state.

From the geometric relationship it can be derived that:

$$M = L \times \cos\left(\frac{\pi}{2} + p\right) \tag{25}$$

where, p is the pitch angle, M is the vertical distance between the two antennas, L is the length of baseline. The vertical distance between the two antennas can be calculated using Equation (25). The corrected water level height can then be determined using Equation (1). Figure 13 shows the change in water level after correction. The root-mean-square error between the corrected water level and the water level obtained through field water gauge

data is 2.46 cm. This is a reduction of 0.03 cm compared to before the correction, indicating that the pitch angle plays a role in improving the accuracy of water level monitoring. Although the improvement in accuracy is small, it provides direction for future research. In the future, we will study the relationship between pitch angle and water level in depth to further improve the accuracy of water level monitoring.

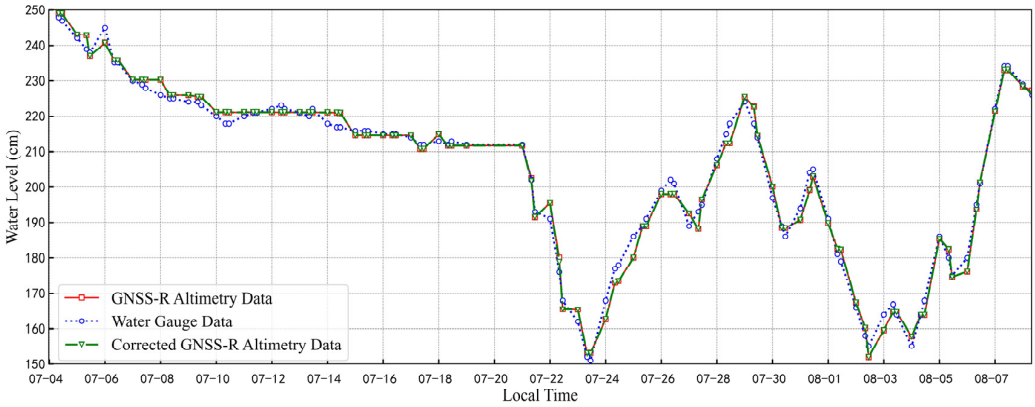


Figure 13. Corrected water level changes for the period 4 July to 8 August 2022.

5. Discussion

In this study, we propose a novel real-time water level monitoring method based on GNSS dual-antenna attitude measurement. Our experimental results demonstrate that our method can achieve real-time water level monitoring for extended periods of time under calm water conditions and can achieve monitoring accuracy at the centimeter level.

We discovered that errors in monitoring results also increased when water levels changed more significantly. We believe this is partly due to a lack of synchronization between the timing of water gauge data and GNSS-R data collection. Water gauge data records water surface height at a specific moment, while GNSS-R data represents the average water surface height over a ten-minute period. As a result, when water levels change more significantly, the discrepancy between GNSS-R data and water gauge data increases. Additionally, multi-path effects may also contribute to this phenomenon. When the amplitude of water surface dynamics is significant, wave motion on the water surface causes multiple reflections of GNSS signals, leading to increased multi-path error and decreased measurement precision.

The multipath error is a significant source of error in carrier phase attitude measurement, with a theoretical maximum of one-fourth of the carrier wavelength [46]. In water level measurement using an LHCP antenna to receive reflected signals from the water surface, multipath effects are the primary cause of measurement inaccuracy. When electromagnetic signals reflect off the surface of the water, they interact with the waves and irregular shapes of the water's surface. As a result, the signals undergo various phenomena, including reflection, refraction, and diffraction, during propagation. These phenomena can cause the signals to travel through multiple paths, which leads to the generation of multipath effects. To achieve millimeter-level accuracy, errors caused by multipath effects must be reduced. Due to the complexity of multipath forms, we plan to introduce a simplified model in future work to simulate the impact of multipath effects on baseline vector solutions through the simulation of actual environmental tests.

As shown in Figure 10, the trends in GNSS-R altimetry data and water scale data from 4 July to 8 August 2022 are generally consistent and accurately reflect changes in water levels. However, between 10 July and 14 July, GNSS-R altimetry results were unable to respond in a timely manner to slight changes in water levels. To determine the cause of this phenomenon, we first examined the raw data from GNSS-R altimetry results. As shown in Figure 14, the number of satellites tracked during this time period was mostly between 30 and 40, indicating that the equipment was functioning properly. Upon further

examination of our algorithm, we discovered issues with baseline processing. Small changes in baseline length, within the range of 1 cm–3 cm, were mistakenly identified as errors and ignored. As a result, the baseline length remained constant from one epoch to another. In future work, we plan to remove this logic to achieve higher accuracy in water level monitoring.

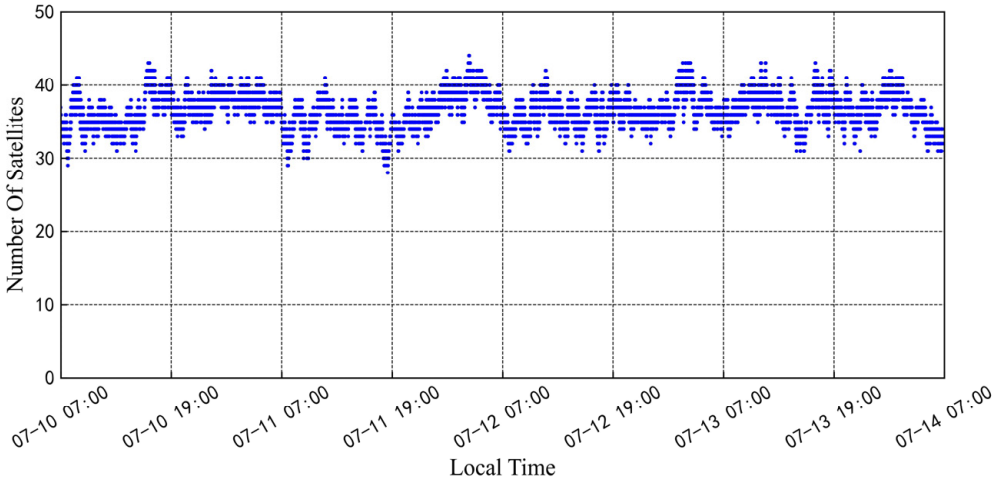


Figure 14. Number of satellites tracked during 10–14 July.

The experimental design of this study has some limitations that warrant further investigation. Firstly, the feasibility of our proposed method was only tested in a single scenario. In future studies, we aim to conduct comparative experiments to examine the impact of various factors such as water depth, distance from the antenna to the water surface, rainfall, satellite elevation angle, and water surface roughness on water level measurement accuracy. This will enable us to establish the robustness and generalizability of our method. Secondly, the receiver we developed was limited by time and financial constraints, which restricted our ability to record data received by both RHCP and LHCP antennas. Consequently, we were unable to perform a post hoc analysis of the data collected. In future studies, we plan to upgrade the receiver to enable the recording of data received by both antennas. This will allow us to analyze the effect of different elevation cutoff angles on the monitoring accuracy and verify the stability of our method under different GNSS systems.

Author Contributions: Conceptualization, Z.P., W.J., J.L. and P.Z.; methodology, Z.P., J.L. and P.Z.; software, Z.P., W.J., J.L. and P.Z.; validation, Z.P., W.J. and P.Z.; formal analysis, P.Z.; investigation, Z.P. and P.Z.; resources, Z.P., P.Z. and M.S.; data curation, M.S. and P.Z.; writing—original draft preparation, P.Z.; writing—review and editing, Z.P., W.J., J.L. and P.Z.; visualization, P.Z.; supervision, Z.P.; project administration, Z.P. All authors have read and agreed to the published version of the manuscript.

Funding: This research was funded by the Beidou Water Conservancy Comprehensive Application Demonstration Project (GFZX030303020127) and China Institute of Water Resources and Hydropower Research Fundamental Research Operation Fund Special Project (JZ110145B0012023, 90022306).

Data Availability Statement: The data set analyzed in this study is managed by the China Institute of Water Resources and Hydropower Research. Corresponding authors can be made available upon request.

Acknowledgments: The authors are grateful for the technical support and assistance provided by Shanghai Sinan Satellite Navigation Technology Company Limited during the experimental period.

Conflicts of Interest: The authors declare no conflict of interest.

References

1. Zhu, D.; Li, H.; Wang, X. Application Prospects of GNSS Remote Sensing Technique in the Development of Smart Water Conservancy. *Water Resour. Hydropower Eng.* **2022**, *15*, 40.
2. Yang, D.; Zhang, Q. *GNSS Reflected Signal Processing: Fundamentals and Applications*; Publishing House of Electronic Industry: Beijing, China, 2012.
3. Foti, G.; Gommenginger, C.; Jales, P.; Unwin, M.; Shaw, A.; Robertson, C.; Rosello, J. Spaceborne gnss reflectometry for ocean winds: First results from the uk techdemosat-1 mission. *Geophys. Res. Lett.* **2015**, *42*, 5435–5441. [CrossRef]
4. Clarizia, M.-P.; Ruf, C.; Cipollini, P.; Zuffada, C. First spaceborne observation of sea surface heightusing GPS-Reflectometry. *AGU Geophys. Res. Lett.* **2016**, *43*, 767–774. [CrossRef]
5. Fabra, F. GNSS-R as A Source of Opportunity for Remote Sensing of the Cryosphere. Ph.D. Thesis, Universitat Politècnica de Catalunya, Barcelona, Spain, 2014.
6. Chew, C.; Shah, R.; Zuffada, C.; Hajj, G.; Masters, D.; Mannucci, A.J. Demonstrating soil moisture remote sensing with observations from the UK TechDemoSat-1 satellite mission. *Geophys. Res. Lett.* **2016**, *43*, 3317–3324. [CrossRef]
7. Zhongmin, M.; Shuangcheng, Z.; Qi, L.; Guanwen, H.; Qiancheng, K.; Jilun, P. Monitoring water level change of the Yellow River by universal GPS receivers. *Nanjing Xinxi Gongcheng Daxue Xuebao* **2021**, *13*, 187–193.
8. Martín-Neira, M. A Passive reflectometry and interferometry system (PARIS): Application to ocean altimetry. *ESA J.* **1993**, *17*, 331–335.
9. Anderson, K.D. Determination of water level and tides using interferometric observations of GPS signals. *J. Atmos. Ocean. Technol.* **2000**, *17*, 1118–1127. [CrossRef]
10. Martin-Neira, M.; Caparrini, M.; Font-Rossello, J.; Lannelongue, S.; Vallmitjana, C. The PARIS concept: An experimental demonstration of sea surface altimetry using GPS reflected signals. IEEE Trans. *Geosci. Remote Sens.* **2001**, *39*, 142–150. [CrossRef]
11. Ruffini, G.; Caparrini, M.; Ruffini, L. PARIS Altimetry with L1 Frequency Data from the Bridge 2 Experiment. *arXiv* **2002**, arXiv:0212055.
12. Wang, X.; He, X.; Zhang, Q. Evaluation and combination of quad-constellation multi-GNSS multipath reflectometry applied to sea level retrieval. *Remote Sens. Environ.* **2019**, *231*, 111229. [CrossRef]
13. Xu, L.; Wan, W.; Chen, X.; Zhu, S.; Liu, B.; Hong, Y. Spaceborne GNSS-R Observation of Global Lake Level: First Results from the TechDemoSat-1 Mission. *Remote Sens.* **2019**, *11*, 1438. [CrossRef]
14. Ha, M.C. Evolution of Soil Moisture and Analysis of Fluvial Altimetry Using GNSS-R. Ph.D. Thesis, Université Paul Sabatier-Toulouse III, Toulouse, France, 2018.
15. Song, M.; He, X.; Wang, X.; Zhou, Y.; Xu, X. Study on the quality control for periodogram in the determination of water level using the GNSS-IR technique. *Sensors* **2019**, *19*, 4524. [CrossRef]
16. Gao, F.; Xu, T.; Wang, N.; He, Y.; Luo, X. A shipborne experiment using a dual-antenna reflectometry system for GPS/BDS code delay measurements. *J. Geod.* **2020**, *94*, 88. [CrossRef]
17. Semmling, M. Altimetric Monitoring of Disko Bay Using Interferometric GNSS Observations on L1 and L2. Ph.D. Thesis, Deutsches GeoForschungsZentrum GFZ, Potsdam, Germany, 2012; 136p.
18. Larson, K.M.; Löfgren, J.S.; Haas, R. Coastal sea level measurements using a single geodetic GPS receiver. *Adv. Space Res.* **2013**, *51*, 1301–1310. [CrossRef]
19. Löfgren, J.S.; Haas, R.; Scherneck, H.G. Sea level time series and ocean tide analysis from multipath signals at five GPS sites in different parts of the world. *J. Geodyn.* **2014**, *80*, 66–80. [CrossRef]
20. Larson, K.M.; Ray, R.D.; Williams, S.D.P. A 10-year comparison of water levels measured with a geodetic GPS receiver versus a conventional tide gauge. *J. Atmos. Ocean. Technol.* **2017**, *34*, 295–307. [CrossRef]
21. Wang, N.; Xu, T.; Gao, F.; Xu, G. Sea level estimation based on GNSS dual-frequency carrier phase linear combinations and SNR. *Remote Sens.* **2018**, *10*, 470. [CrossRef]
22. Wang, X.; He, X.; Xiao, R.; Song, M.; Jia, D. Millimeter to centimeter scale precision water-level monitoring using GNSS reflectometry: Application to the South-to-North Water Diversion Project, China. *Remote Sens. Environ.* **2021**, *265*, 112645. [CrossRef]
23. Wang, F.; Zhang, B.; Yang, D.; Xing, J.; Zhang, G.; Yang, L. Four-Channel Interference of Dual-Antenna GNSS Reflectometry and Water Level Observation. *IEEE Geosci. Remote Sens. Lett.* **2021**, *19*, 8019305. [CrossRef]
24. Martín-Neira, M.; Colmenarejo, P.; Ruffini, G.; Serra, C. Altimetry precision of 1 cm over a pond using the wide-lane carrier phase of GPS reflected signals. *Can. J. Remote Sens.* **2002**, *28*, 394–403. [CrossRef]
25. Löfgren, J.S.; Haas, R. Sea Level Measurements Using Multi-Frequency GPS and GLONASS Observations. *EURASIP J. Adv. Signal Process.* **2014**, *2014*, 50. [CrossRef]
26. Liu, W.; Beckheinrich, J.; Semmling, M.; Ramatschi, M.; Vey, S.; Wickert, J.; Hobiger, T.; Haas, R. Coastal Sea-Level Measurements Based on GNSS-R Phase Altimetry: A Case Study at the Onsala Space Observatory, Sweden. *IEEE Trans. Geosci. Remote Sens.* **2017**, *55*, 5625–5636. [CrossRef]
27. Fabra, F.; Cardellach, E.; Rius, A.; Ribo, S.; Oliveras, S.; Nogués-Correig, O.; Rivas, M.B.; Semmling, M.; D'Addio, S. Phase altimetry with dual polarization GNSS-R over sea ice. *IEEE Trans. Geosci. Remote Sens.* **2011**, *50*, 2112–2121. [CrossRef]
28. He, Y.; Gao, F.; Xu, T.; Meng, X.; Wang, N. Coastal altimetry using interferometric phase from GEO satellite in quasi-zenith satellite system. *IEEE Geosci. Remote Sens. Lett.* **2021**, *19*, 3002505. [CrossRef]

29. Kucwaj, J.C.; Reboul, S.; Stienne, G.; Choquel, J.B.; Benjelloun, M. Circular Regression Applied to GNSS-R Phase Altimetry. *Remote Sens.* **2017**, *9*, 651. [CrossRef]
30. Bao, L.F.; Wang, N.Z.; Gao, F. Improvement of Data Precision and Spatial Resolution of cGNSS-R Altimetry Using Improved Device with External Atomic Clock. *IEEE Geosci. Remote Sens.* **2016**, *13*, 207–211. [CrossRef]
31. Zhao, L.; Li, N.; Li, L.; Zhang, Y.; Chun, C. Real-Time GNSS-Based Attitude Determination in the Measurement Domain. *Sensors* **2017**, *17*, 296. [CrossRef]
32. Wang, N.Z.; Bao, L.F.; Gao, F. Improved Water Level Retrieval from Epoch-by-Epoch Single and Double Difference GNSS-R Algorithms. *Acta Geod. Er Cartogr. Sinica.* **2016**, *45*, 795–802.
33. Rius, A.; Nogués-Correig, O.; Ribó, S.; Cardellach, E.; Oliveras, S.; Valencia, E.; Park, H.; Tarongi, J.M.; Camps, A.; van der Marel, H.; et al. Altimetry with GNSS-R interferometry: First proof of concept experiment. *GPS Solut.* **2012**, *16*, 231–241. [CrossRef]
34. Masters, D. *Surface Remote Sensing Applications of GNSS Bistatic Radar: Soil Moisture and Aircraft Altimetry*; University of Colorado: Boulder, CO, USA, 2004.
35. Kaplan, E. *Understanding GPS—Principles and Applications*, 2nd ed.; Artech House: Norwood, MA, USA, 2005.
36. Teunissen, P.J.G. An Optimality Property of the Integer Least-Squares Estimator. *J. Geod.* **1999**, *73*, 587–593. [CrossRef]
37. Xu, G.; Xu, Y. Applications of GPS Theory and Algorithms. In *GPS*; Springer: Berlin/Heidelberg, Germany, 2016.
38. Teunissen, P.J.G.; Montenbruck, O. *Springer Handbook of Global Navigation Satellite Systems*; Springer International Publishing: Cham, Switzerland, 2017.
39. Frei, E.; Beutler, G. Rapid static positioning based on the fast ambiguity resolution approach 'FARA' theory and first results. *Manuscr. Geod.* **1990**, *15*, 325–356.
40. Euler, H.-J.; Schaffrin, B. On a Measure for the Discernibility between Different Ambiguity Solutions in the Static-Kinematic GPS-Mode. In *International Association of Geodesy Symposia*; Springer: Berlin/Heidelberg, Germany, 1991; Volume 107, pp. 285–295.
41. Tiberius, C.C.; De Jonge, P. Fast positioning using the LAMBDA method. In Proceedings of the International Symposium on Differential Satellite Navigation Systems, Bergen, Norway, 24–28 April 1995; pp. 24–28.
42. Han, S. Quality-control issues relating to instantaneous ambiguity resolution for real-time GPS kinematic positioning. *J. Geodesy* **1997**, *71*, 351–361. [CrossRef]
43. Song, F. Research on GNSS Integer Ambiguity Estimation Methods. Ph.D. Thesis, China University of Mining & Technology, Beijing, China, 2016.
44. Zhang, Y.; Tian, L.; Meng, W.; Gu, Q.; Han, Y.; Hong, Z. Feasibility of code-level altimetry using coastal BeiDou reflection (BeiDou-R) setups. *IEEE J. Stars* **2015**, *8*, 4130–4140. [CrossRef]
45. Medina, D.; Heßelbarth, A.; Büscher, R.; Ziebold, R.; García, J. On the Kalman filtering formulation for RTK joint positioning and attitude quaternion determination. In Proceedings of the 2018 IEEE/ION Position, Location and Navigation Symposium (PLANS), Monterey, CA, USA, 23–26 April 2018; pp. 597–604.
46. Lau, L.; Cross, P. Development and testing of a new ray-tracing approach to GNSS carrier-phase multipath modelling. *J. Geodesy* **2007**, *81*, 713–732. [CrossRef]

Disclaimer/Publisher's Note: The statements, opinions and data contained in all publications are solely those of the individual author(s) and contributor(s) and not of MDPI and/or the editor(s). MDPI and/or the editor(s) disclaim responsibility for any injury to people or property resulting from any ideas, methods, instructions or products referred to in the content.